OPTICS

Color-pure red light-emitting diodes based on two-dimensional lead-free perovskites

Fanglong Yuan[1,2]*, Xiaopeng Zheng[3]*, Andrew Johnston[1]*, Ya-Kun Wang[1]*, Chun Zhou[1], Yitong Dong[1], Bin Chen[1], Haijie Chen[1], James Z. Fan[1], Geetu Sharma[4], Peicheng Li[2], Yuan Gao[1], Oleksandr Voznyy[4], Hao-Ting Kung[2], Zheng-Hong Lu[2]†, Osman M. Bakr[3]†, Edward H. Sargent[1]†

Copyright © 2020 The Authors, some rights reserved; exclusive licensee American Association for the Advancement of Science. No claim to original U.S. Government Works. Distributed under a Creative Commons Attribution NonCommercial License 4.0 (CC BY-NC).

It remains a central challenge to the information display community to develop red light-emitting diodes (LEDs) that meet demanding color coordinate requirements for wide color gamut displays. Here, we report high-efficiency, lead-free $(PEA)_2SnI_4$ perovskite LEDs (PeLEDs) with color coordinates (0.708, 0.292) that fulfill the Rec. 2100 specification for red emitters. Using valeric acid (VA)—which we show to be strongly coordinated to Sn^{2+}—we slow the crystallization rate of the perovskite, improving the film morphology. The incorporation of VA also protects tin from undesired oxidation during the film-forming process. The improved films and the reduced Sn^{4+} content enable PeLEDs with an external quantum efficiency of 5% and an operating half-life exceeding 15 hours at an initial brightness of 20 cd/m^2. This work illustrates the potential of Cd- and Pb-free PeLEDs for display technology.

INTRODUCTION

The advent of wide color gamut displays motivates the development of light-emitting diodes (LEDs) with bright emission and high color purity (*1*, *2*). Lead (Pb)–based perovskites have achieved high color purity and near-theoretical efficiencies for green emitters, and epitaxially grown GaN LEDs have done so in the blue region (*3*, *4*). However, the development of efficient red LEDs with Commission Internationale de l'Eclairage (CIE) color coordinates matching the Rec. 2100 standard—emission centered at 630 nm with a spectral full width at half maximum (FWHM) of <22 nm—remains unrealized (*5*–*11*).

Table 1 summarizes the key optical parameters of currently available red emitters for LEDs. Cd-based and Pb-perovskite–based quantum dots (QDs) have emerged as candidates for red LEDs due to their solution processing, high brightness, and spectral tunability. Unfortunately, the emission peaks are at wavelengths exceeding 640 nm, and the FWHMs are larger than 30 nm (Table 1) (*12*–*14*). In addition, Cd^{2+} and Pb^{2+} are both regulated substances.

Among Pb-free and Cd-free materials, indium-based QDs have efficient emission at 630 nm, but the emission linewidths are broad, typically exceeding 50 nm (*15*). Red organic LEDs suffer from an even broader emission (FWHM, >60 nm) (*16*). Inorganic semiconductor single crystals, such as epitaxially grown GaAs, GaAlAs, and GaAlInP, have also been explored for red LEDs. These nanocrystals have demonstrated narrow FWHMs of ~25 nm; however, the emission is centered in the deep red region (>640 nm) and exhibits asymmetric emission spectra with a color coordinate of (0.70, 0.30) (*17*). There is, thus, substantial interest in developing red LEDs that are efficient, emit at the needed wavelength, and have sufficiently narrow linewidths—all needed simultaneously to meet the Rec. 2100 color coordinate specifications.

In recent years, lead-free tin (Sn) perovskites have emerged as a promising optoelectronic material (*18*–*27*). There are two key challenges in Sn perovskites: Sn^{2+} is prone to oxidation to its tetravalent state (Sn^{4+}), especially when in the precursor solution and during the annealing process for film formation, and the crystallization rate of Sn perovskites is much faster than that of the Pb analogs. Together, these result in high Sn^{2+} vacancy defect densities and poor film morphology and coverage. This results in rapid nonradiative annihilation of excitons and poor charge transport through the film, severely curtailing the performance of Sn-based perovskite LEDs (PeLEDs).

To address the oxidation of Sn^{2+}, one may add reducing agents such as SnF_2, SnF_2-pyrazine complex, Sn powder, and hydroxybenzene sulfonic acid to the precursor solution (*28*–*30*). This has helped advance Sn-based solar cells and photodetectors; however, PeLEDs are even more vulnerable to trap states and to poor film quality. Advances in Sn-based PeLEDs demand a more precise understanding of the oxidation and crystallization kinetics in Sn PeLEDs, and more robust strategies to address these.

Here, we develop a strategy to improve film quality and protect Sn^{2+} from oxidation through the addition of valeric acid (VA). Strong interactions between VA and Sn^{2+} reduce the crystallization rate of the perovskite precursors, improving the final film morphology. Levering the twofold benefit from VA, we fabricate PEA_2SnI_4 LEDs with an external quantum efficiency (EQE) of 5% and an operating half-life exceeding 15 hours, with color coordinates matching the Rec. 2100 specification for a primary red emitter. This is the highest efficiency and stability reported among lead-free PeLEDs reported to date.

RESULTS

Interactions between VA and perovskite

We sought first to identify the interaction between VA and Sn-based perovskites in both the precursor solution and the solid-state films. We used ^{1}H nuclear magnetic resonance (NMR) and ^{13}C NMR spectroscopy to study the interaction between VA and the Sn-perovskite

[1]Department of Electrical and Computer Engineering, University of Toronto, 35 St George Street, Toronto, Ontario M5S 1A4, Canada. [2]Department of Materials Science and Engineering, University of Toronto, 184 College Street, Toronto, Ontario M5S 3E4, Canada. [3]Division of Physical Sciences and Engineering, King Abdullah University of Science and Technology (KAUST), Thuwal 23955-6900, Kingdom of Saudi Arabia. [4]Department of Physical and Environmental Sciences, University of Toronto, Scarborough 1065 Military Trail, Toronto, Ontario M1C 1A4, Canada.
*These authors contributed equally to this work.
†Corresponding author. Email: zhenghong.lu@utoronto.ca (Z.-H.L.); osman.bakr@kaust.edu.sa (O.M.B.); ted.sargent@utoronto.ca (E.H.S.)

Downloaded from http://advances.sciencemag.org/ on November 30, 2020

Table 1. Key optical parameters of red emitters for LED applications.

Materials category and example		Emission peak (nm)	FWHM (nm)	CIE	Distance to Rec. 2100	Reference
Cd-based QDs	CdSe@CdS	640	30	(0.71, 0.29)	0.003	(*12*)
Pb-based QDs	$CsPb(Br/I)_3$	649	33	(0.72, 0.28)	0.017	(*13*)
	$CsPbI_3$	675	40	NA	NA	(*14*)
In-based QDs	InP/ZnSe/ZnS	630	50–60	(0.69, 0.31)	0.026	(*15*)
Organic molecule	DBP	610	>60	(0.61, 0.39)	0.14	(*16*)
Inorganic semiconductors	GaAlAs	>640	>25	(0.72, 0.28)	0.017	(*17*)
Sn-based	PEA_2SnI_4	632	21	(0.708, 0.292)	0	This work

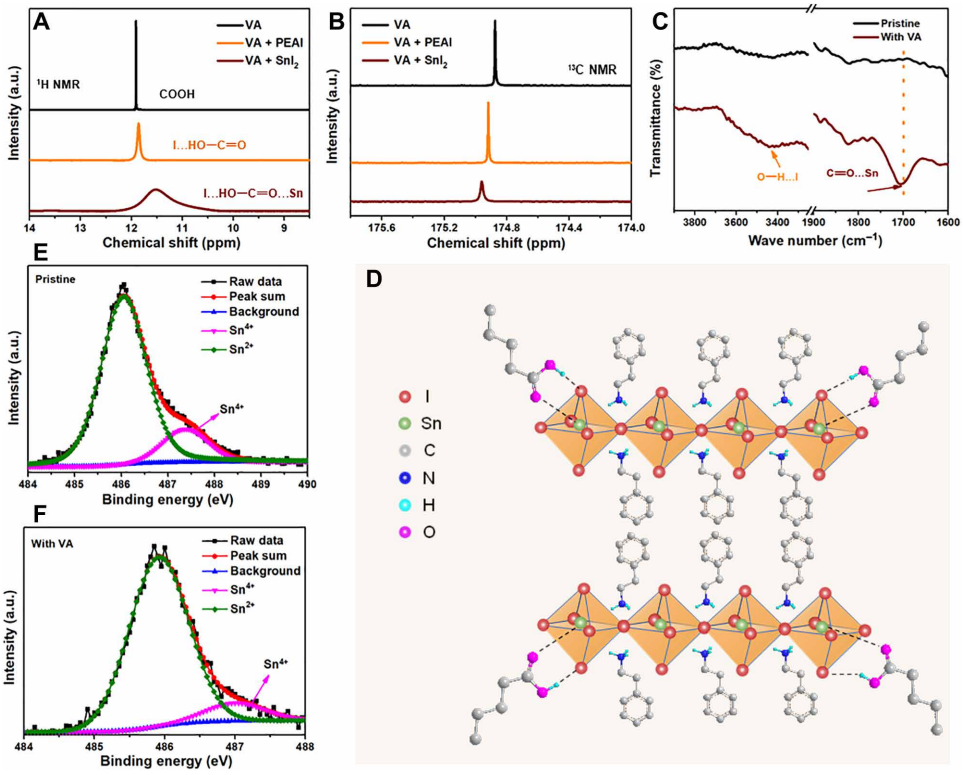

Fig. 1. Interactions between VA and perovskite precursors and perovskite films. ^{1}H NMR (**A**) and ^{13}C NMR (**B**) spectra of VA, VA + PEAI, and VA + SnI_2 in DMSO-d_6 solution. a.u., arbitrary unit. (**C**) FTIR spectra of PEA_2SnI_4 film prepared with and without VA. (**D**) Representation of hydrogen bonding (O—H···I) and coordination bonding (C=O···Sn) interactions between VA and PEA_2SnI_4 crystals. High-resolution Sn3d XPS spectra of PEA_2SnI_4 films prepared with (**F**) and without (**E**) VA. Pristine films were prepared with the precursors containing metallic Sn powder.

precursor (Fig. 1, A and B). The Sn-perovskite precursor is typically formed by dissolving PEAI (phenethylammonium iodide) and SnI_2 in a mixture of *N*,*N*′-dimethylformamide (DMF) and dimethyl sulfoxide (DMSO).

We first probed a sample containing only VA in deuterated DMSO-d_6. We observed a resonance signal with a chemical shift at 11.2 parts per million (ppm), which we attribute to the active hydrogen in the carboxylic group of VA. We then added PEAI to the VA solution and noted that the signal was broadened, indicating that a O=C—OH···I^- hydrogen bond was formed (Fig. 1A). The broad linewidths indicate that the VA molecule is immobilized by the strong O=C—OH···I^- hydrogen bond. Conversely, when VA was added to a solution of PEAI dissolved in DMSO, the resonance signals of NH_2 and CH_2 in PEA^+ were not obviously changed, indicating that the interaction between PEA^+ and VA is weak and that the hydrogen bonding is from the O=C—OH···I^- interaction (fig. S1) (*31*).

We added SnI_2 to the VA solution and noted that the broadening of the VA signal is much greater than when PEAI is added (Fig. 1A). This indicates that in addition to the hydrogen bonding between VA and I^-, there is also strong interaction between VA and Sn^{2+} in the form of HO—C=O···Sn^{2+}. This is also observed in ^{13}C NMR spectroscopy (Fig. 1B and fig. S2).

Downloaded from http://advances.sciencemag.org/ on November 30, 2020

The presence of VA in the final film and its interactions with perovskite were probed using Fourier transform infrared spectroscopy (FTIR). A broad stretching vibration band in the range of 3400 to 3200 cm^{-1} appears in perovskite films prepared with VA, indicating strong hydrogen bonding (O—H···I) between VA and the perovskite (Fig. 1C) (*32*–*35*). A distinct stretching vibration at 1700 cm^{-1} is also observed in the perovskite film at a wave number lower than that of the stretching vibration band of C═O in a carboxylic group (1720 to 1760 cm^{-1}). This indicates strong bonding interactions between VA and Sn^{2+} (HO—C═O···Sn^{2+}) in the final perovskite films. The shift of the stretching vibration band of C═O is caused by the lone pair of electrons on the carboxylic group of VA interacting with the empty orbital of Sn^{2+} in the perovskite film. Note that the VA molecules cannot be incorporated into the perovskite lattice; instead, they remain on the surface of PEA_2SnI_4 films. Figure 1D illustrates schematically the hydrogen bonding (O═C—OH···I^-) and coordination bonding (C═O···Sn^{2+}) interactions between VA and perovskite film.

We acquired x-ray photoelectron spectra (XPS) to further evaluate Sn^{2+} oxidation in the PEA_2SnI_4 films with the introduction of VA. We prepared perovskite precursors according to a reported method in which metallic Sn powder (Sn^0) is added to the precursor solution to reduce Sn^{4+} content through a comproportionation reaction, and we use it as a baseline for the following studies. We find that the Sn^{4+} content of the PEA_2SnI_4 films made using the precursor containing Sn^0 is reduced from 26 atomic % (at %) (for the film made from a precursor solution without Sn^0) to 16 at % (Fig. 1E and fig. S3, A and B). However, even with this strategy to reduce Sn^{4+} content in precursor solution, the resulting films still show a high Sn^{4+} content—which we explain by noting that Sn^{2+} oxidation occurs continuously in film processing and final solid-state perovskite films. XPS confirms that the Sn^{4+} content is further reduced to 7 at % for the PEA_2SnI_4 films prepared with VA (Fig. 1E). This indicates that the VA may serve to inhibit the oxidation of tin during film formation as a result of the VA-perovskite coordination (fig. S3, C and D). From top view scanning electron microscopy (SEM) images of the different films, it is seen that the film morphology is improved upon the addition of VA (Fig. 2, A and B). The decreased grain size for the VA-containing sample may also limit the degree to which the perovskite is exposed to O_2, which will also inhibit oxidation. Together, the small grain size and VA-perovskite interaction do inhibit Sn oxidation, but the individual effects of each phenomenon are difficult to deconvolve. Pristine PEA_2SnI_4 perovskite films had large grains and poor film coverage with many pinholes (Fig. 2A). The existence of pinholes and poor film coverage for the PEA_2SnI_4 films was due to the fast crystal growth before the nucleation being complete. However, when VA was added, we formed homogeneous films with no pinholes (Fig. 2B). We postulate that the interaction between the VA and Sn-perovskite precursors inhibits the rate of film crystallization, allowing the nucleation of crystals to complete before grains had grown to become overly large. This is supported by the decreased grain sizes: Without VA, the grain sizes were broadly distributed in the range of 400 to 4000 nm, while the VA-containing samples had a more uniform film with very small grain size (fig. S4). Atomic force microscopy (AFM) images also highlight the improved film quality of PEA_2SnI_4 perovskite films prepared with VA

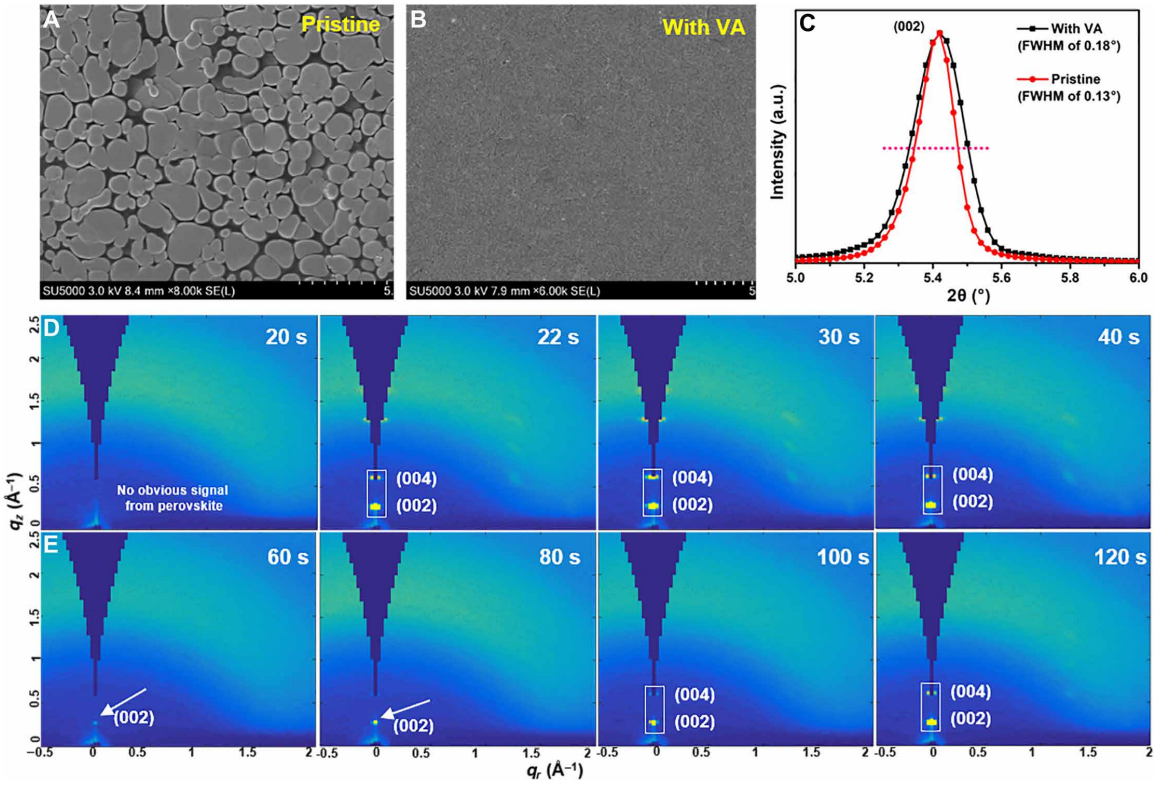

Fig. 2. Crystallization kinetics and structural characterization of PEA_2SnI_4 films. SEM image of PEA_2SnI_4 films prepared without (**A**) and with (**B**) VA. (**C**) High-resolution XRD spectra (in the range from 5° to 6°) of PEA_2SnI_4 films prepared with and without VA. In situ GIWAXS measurements of spin-coated PEA_2SnI_4 without (**D**) and with (**E**) VA at different times.

Downloaded from http://advances.sciencemag.org/ on November 30, 2020

(fig. S5). The result illustrates that, in addition to superior suppression of oxidation of Sn^{2+}, VA also tunes the crystallization kinetics and improves film morphology, which can improve the optoelectronic properties of the films. We note that the inclusion of the VA has negligible impact on the wettability of the precursor solution, indicating that the improved homogeneity was rather a result of the interaction of VA with the precursor constituents (*36*).

Encouraged by the improved film quality, we sought to identify the differences in the crystallization of PEA_2SnI_4 perovskite films with and without VA. We investigated the evolution of grazing incidence wide-angle x-ray scattering (GIWAXS) diffraction patterns during film deposition (*37*). The in situ GIWAXS images clearly depict the fast crystal growth of films prepared without VA (Fig. 2D). In films without VA, strong diffractions corresponding to the (002) and (004) planes appeared simultaneously at 22 s (Fig. 2B and fig. S6). However, when VA was added into the PEA_2SnI_4 perovskite precursor solution, film crystallization rate was substantially slower. We observe weak signals of (002) diffraction only at 60 s, which gradually strengthens over the next 20 s (Fig. 2E). After an additional 20 s, the signal of (004) diffraction emerges, and this peak also gradually becomes stronger (Fig. 2E). This indicates that the VA retards the crystal growth, a finding we assign to the strong interaction between VA and the perovskite precursors via O═C─$OH^{\cdots}I^{-}$ and HO─C═$O^{\cdots}Sn^{2+}$ (Fig. 1, A to C), inhibiting thereby fast nucleation. The slower crystallization leads to a more uniform nucleation and forms a homogeneous and pinhole-free film. In both cases, the perovskite crystals align parallel to the substrate, as reported for $n = 1$ perovskites. Each film for the in situ GIWAXS study was processed in exactly the same way (Materials and Methods). X-ray diffraction (XRD) patterns of PEA_2SnI_4 perovskite films prepared with and without VA show similar peaks, which are assigned to strong (00*l*) diffractions (fig. S7). The integrated GIWAXS patterns of perovskite films are well matched with the findings from XRD (fig. S7E), indicating that there are no substantial differences between the bulk and surface crystallinity. We also find that the addition of VA leads to broader (00l) diffraction peaks. The (002) diffraction peaks of samples prepared with VA have a FWHM of 0.18°, compared with 0.13° for samples prepared without VA (Fig. 2C). This indicates that the PEA_2SnI_4 perovskite has a lower crystallinity when crystallized in the presence of VA, agreeing with the smaller grain sizes seen in SEM images.

Optical properties and carrier dynamics

The PEA_2SnI_4 films prepared with VA show a narrow excitonic absorption peak centered at 612 nm and a photoluminescence (PL) emission peak centered at ~630 nm (Fig. 3A), which is blue shifted ~10 nm compared with that of PEA_2SnI_4 films prepared without VA (fig. S8A). The slightly blue-shifted emission peak may result from the reduced trap emission of PEA_2SnI_4 films prepared with VA. The quantum yield (QY) of PEA_2SnI_4 films increased sevenfold from 1.0 ± 0.3% (pristine) to 7 ± 3% (with VA), which we ascribe to reduced Sn^{2+} vacancies and trap states.

To gain further insight into exciton recombination dynamics, we measured time-resolved PL spectra of PEA_2SnI_4 films prepared with and without VA and find that these fit well to biexponential decay curves (Fig. 3B and table S1). The biexponential decay behavior suggests that there are two different species involved in the emission. We ascribe the short-lived PL lifetime probably to surface recombination,

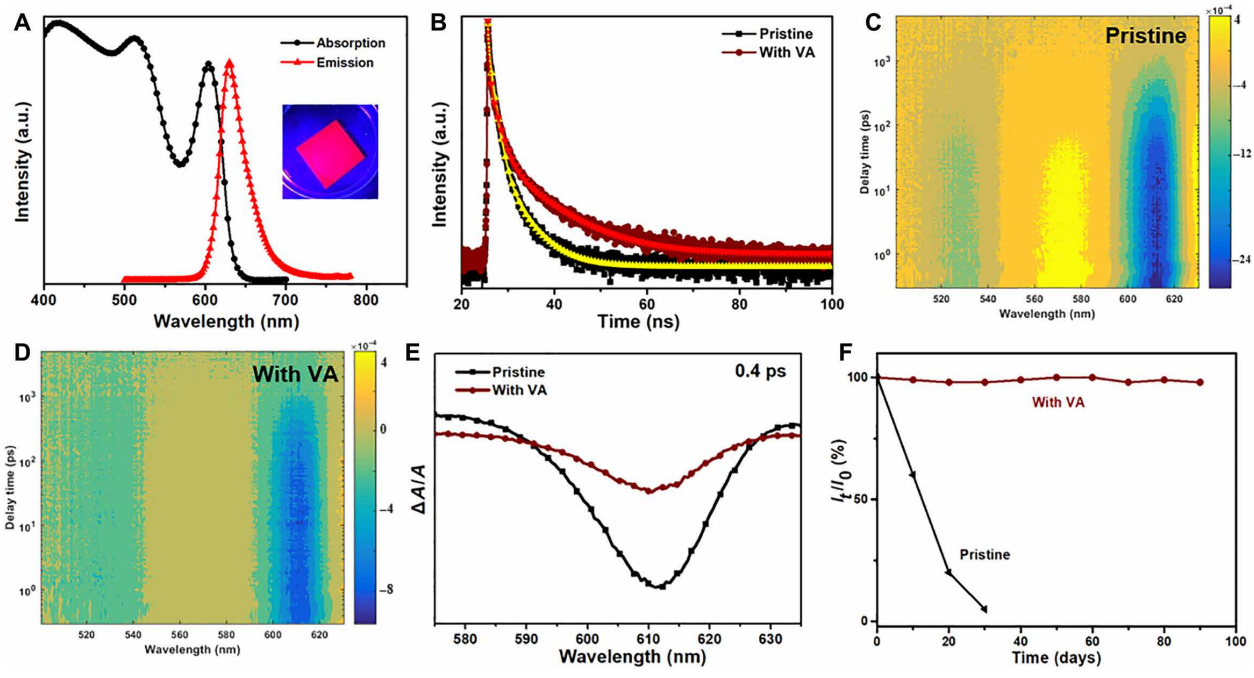

Fig. 3. Optical properties and carrier dynamics in PEA_2SnI_4. (**A**) Absorption and PL spectra of PEA_2SnI_4 films (inset shows the light emission image under UV light excitation). (**B**) Time-resolved PL and corresponding fits of PEA_2SnI_4 films prepared with and without VA. Two-dimensional pseudocolor map of fs-TA spectra of PEA_2SnI_4 films prepared without (**C**) and with (**D**) VA expressed as ΔOD (the change of the absorption intensity of the sample after excitation at 650 nm) as a function of both delay time and probe wavelength. (**E**) TA signal of PEA_2SnI_4 films at 612 nm with an excitation wavelength of 650 nm at a corresponding delay time of 0.4 ps. Here, the ΔOD is normalized to the linear OD at each wavelength to allow for quantitative comparison. (**F**) The normalized emission intensity of PEA_2SnI_4 films prepared with and without VA after storing for 3 months.

Downloaded from http://advances.sciencemag.org/ on November 30, 2020

while the longer lifetime is ascribed to bulk recombination (*38*). Upon the addition of VA, the average fluorescence lifetime of PEA_2SnI_4 films increases from 0.8 to 1.9 ns (table S1). The QY is determined by the ratio of the radiative recombination rate (k_{rad}) to the sum of radiative and nonradiative (k_{non}) recombination rates (k_{tot})

$$\text{PLQY} = \frac{k_{rad}}{k_{tot}} = \frac{k_{rad}}{k_{rad} + k_{non}}$$

in which the lifetime $\tau = 1/(k_{rad} + k_{non})$. Thus, k_{rad} and k_{non} can be deduced from the PLQY: The calculated values are listed in table S1. k_{rad} was increased in the PEA_2SnI_4 films prepared with VA, potentially a result of increased binding energy associated with smaller grain sizes (*38*). In addition, k_{non} was also greatly suppressed in the PEA_2SnI_4 films.

We carried out femtosecond transient absorption (fs-TA) measurements on perovskite films with and without VA. We use a 650-nm pump pulse to excite PEA_2SnI_4 films at sub-bandgap energy. In this case, electrons from the valence band can only be excited to midgap trap states, and the bleach signal at the excitonic energy is thus proportional to the density of trap states. In this way, sub-bandgap narrowband TA offers a way to compare relative trap state densities when the bleach signal is normalized to the steady-state optical density (*39*). The two-dimensional pseudocolor maps of the intensity change in the TA signal as a function of both delay time and probe wavelength are shown in Fig. 3C (PEA_2SnI_4 films prepared without VA) and Fig. 3D (PEA_2SnI_4 films prepared with VA). The lifetimes of the bleach at 612 nm are similar, indicating that the lifetime of trapped electrons is the same; we find that the PEA_2SnI_4 films without VA exhibit a much higher bleach intensity at 612 nm compared with PEA_2SnI_4 films prepared with VA (Fig. 3E and fig. S8B). This indicates that the VA reduces the trap state density in the Sn-perovskite films, which is manifested in a longer carrier lifetime and higher PLQY.

The TA bleach dynamics of the PEA_2SnI_4 films prepared with VA at the band edge (612 nm) show a slower recovery compared with that of the PEA_2SnI_4 films without VA (fig. S8C). This agrees with a picture in which trap densities in the PEA_2SnI_4 films prepared with VA are reduced, consistent with the increased PLQY and increased average lifetime observed in the PL decay traces.

We also studied the stability of PEA_2SnI_4 films in ambient glovebox conditions: The emission intensity and spectra of films prepared with VA show no obvious change after being stored for 3 months; films prepared without VA show almost no emission after 1 month (Fig. 3F). This indicates that the oxidation of the perovskite is inhibited even after film formation, a finding we ascribe to both the VA bound to the perovskite surface and the decreased grain size of the film.

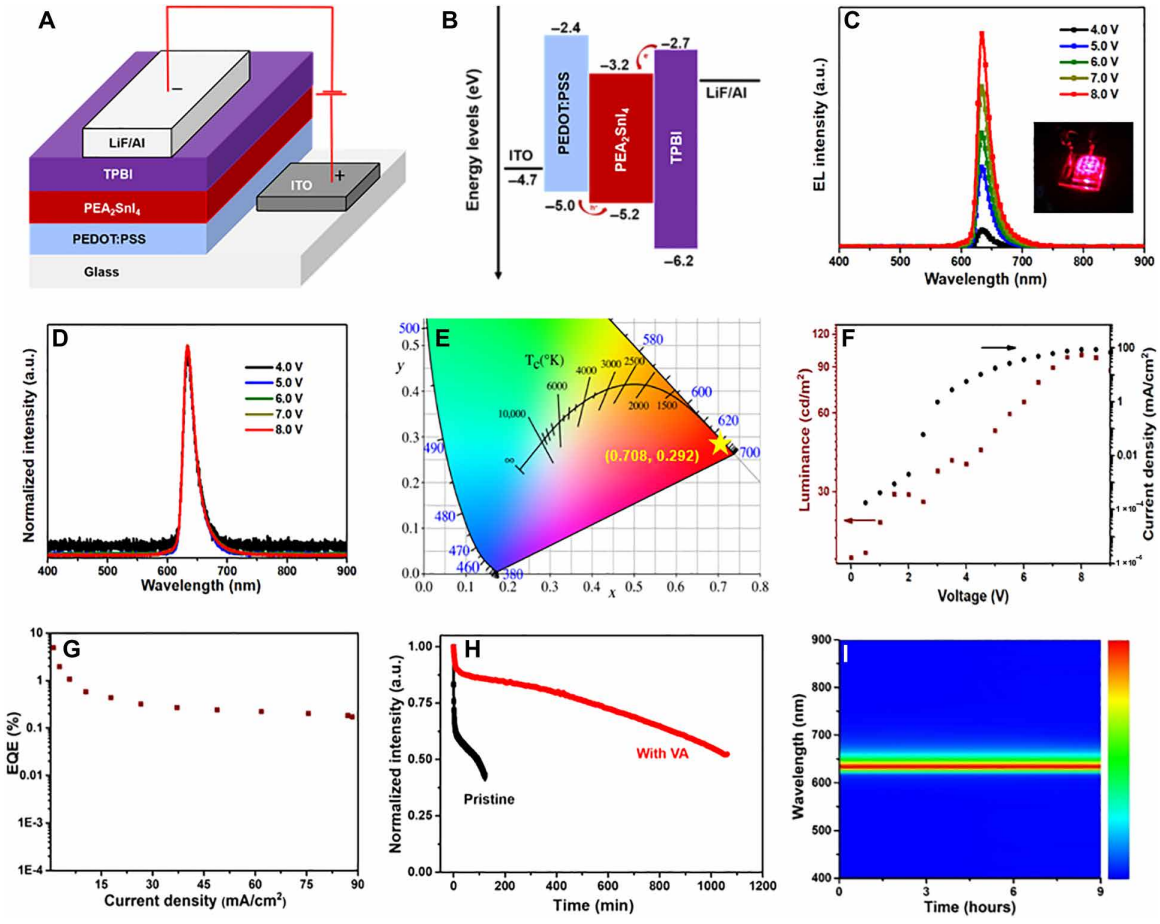

Fig. 4. LED structure, energy diagram, and performance. (**A**) Device structure, (**B**) energy level diagram, (**C**) EL spectra, and (**D**) normalized EL spectra of PEA_2SnI_4 LEDs at different operation voltage. (Inset is the operation photograph of the red LEDs operated at 7 V.) (**E**) Color coordinate in the CIE 1931 chromaticity diagram of the EL spectra. (**F**) Luminance–voltage–current density and (**G**) EQE–current density characteristics, and (**H**) operational lifetimes and (**I**) emission spectra as functions of device operation time.

Downloaded from http://advances.sciencemag.org/ on November 30, 2020

This strategy can be generally applied to other Sn-based perovskites: The emission intensities of PEA_2SnI_3Br and $PEA_2SnI_2Br_2$ were also improved more than 10-fold upon the addition of VA (fig. S9).

Device structure and performance

We sought to lever these improved photoluminescent properties and film morphology to fabricate PEA_2SnI_4 LEDs. We use an indium tin oxide (ITO) glass substrate anode, a poly(3,4-ethylenedioxythiophene): poly(styrene sulfonate) (PEDOT:PSS) hole injection layer (HIL), an active PEA_2SnI_4 emission layer, a 1,3,5-tris(*N*-phenylbenzimidazol-2-yl) benzene (TPBI) electron transport layer, and a lithium fluoride (LiF)/Al double-layered cathode (Fig. 4A). As illustrated in the energy level diagram of the PEA_2SnI_4-based LEDs shown in Fig. 4B, the valence band maximum energy is 5.22 eV, which is obtained by summing the work function and valence band maximum binding energy, both measured from ultraviolet photoelectron spectroscopy (UPS) (fig. S10, A and B). The conduction band minimum energy is obtained by adding the optical bandgap, which is calculated from the edge of the absorption spectrum (fig. S10C).

The emission peaks of electroluminescence (EL) spectra of the PEA_2SnI_4-based LEDs are centered at 632 nm (Fig. 4C) and show no obvious change under different voltage operation (Fig. 4D). The FWHM of the EL spectrum is 21 nm, narrower than state-of-the-art red LEDs. The color coordinate of the LED is (0.708, 0.292), exactly matching the Rec. 2100 specifications for a primary red emitter (Fig. 4E). Luminance and current density as a function of applied voltage are shown in Fig. 4F. The maximum EQE is 5% (the corresponding brightness is 38 cd/m^2) (Fig. 4G and fig. S11, A and B), exceeding that of all previously reported lead-free perovskite-based LEDs (*40*). The EQE is also 50 times higher than LEDs made without VA. The EQE histograms of LED devices treated with and without VA show corresponding average EQEs of 3.1 and 0.13%, respectively (fig. S11, C and D). The PEA_2SnI_4-based LEDs show a half-lifetime exceeding 15 hours, more than 10-fold higher than the control LEDs (Fig. 4H). The improved device stability is ascribed to the strong interactions between VA and the perovskite film, which suppresses ion migration during device operation in addition to preventing tin oxidation. The EL spectra also show no obvious change after operation for 9 hours (Fig. 4I). Using the same strategy, we fabricated mixed halide PEA_2SnI_3Br-based LEDs emitting at 595 nm with a brightness of 380 cd/m^2 (fig. S12A). These devices exhibit stable EL spectra at different applied potentials (fig. S12B), indicating that ion migration is suppressed by the VA: Halide segregation is known to red shift the EL spectra in mixed halide PeLEDs.

DISCUSSION

We report stable and efficient Sn-based PeLEDs that match the Rec. 2100 specifications for primary red emitters. The new method improves film quality and protect Sn^{2+} from oxidation. As a result, we fabricate PeLEDs with record performance of a 5% EQE improving 50-fold compared with control devices and a half-lifetime exceeding 15 hours at an initial brightness of 20 cd/m^2.

MATERIALS AND METHODS

Materials

Chemicals listed below are commercially available and used without further purification. Tin (II) iodide (SnI_2, 99.999%) and metallic Sn powder (100 mesh) were purchased from Alfa Aesar. PEAI, VA solution (>99%), toluene (anhydrous, 99.8%), DMF (anhydrous, 99.8%), DMSO (anhydrous, ≥99.9%), and LiF were purchased from Sigma-Aldrich. PEDOT:PSS (AI 4083) was purchased from Heraeus. Aluminum pellet and TPBI were purchased from Lumtec.

PEA_2SnI_4 film preparation

The PEA_2SnI_4 films prepared with or without VA were spin coated via a two-step process, 1000 revolutions per minute (rpm) for 10 s (accelerated speed is 200) and then 5000 rpm for 60 s (accelerated speed is 800). At the last 10 s in the second step, 300 μl of anti-solvent toluene was dropped quickly, followed by annealing in a nitrogen-filled glovebox at 100°C for 10 min to form the perovskite films. For film characterization, XPS and UPS measurements were conducted on a Si substrate, and other measurements were conducted on an ITO substrate.

Optical characterization

Steady-state PL spectra was recorded using a HORIBA Fluorolog system equipped with a single grating, and a monochromatized Xe lamp was used as the excitation source. PLQY measurements were done by coupling a Quanta-phi integrating sphere to the HORIBA Fluorolog system with optical fiber bundles. Both excitation and emission spectra were collected for the two cases of the sample directly illuminated by the excitation beam path in the integrating sphere and the empty sphere itself. A time-correlated single photon counting detector and a pulsed UV laser diode (λ = 374 nm) were used to acquire time-resolved PL spectra. An instrument response function of Δt = 0.13 ns provides a limit to the overall time resolution. Time-resolved emission spectra were recorded by measuring individual transient PL traces at increasing emission wavelengths. UV–visible (vis) absorption was measured using a LAMBDA 950 UV/Vis/NIR spectrometer (*34*).

fs-TA measurement

A Yb:KGW regenerative amplifier (Pharos, Light Conversion) produced the 1030-nm fundamental (5 kHz). A portion of the beam was passed through an optical parametric amplifier (Orpheus, Light Conversion) to generate the 3.8-eV pump pulse. Both the pump pulse and residual fundamental were sent into an optical bench (Helios, Ultrafast). The fundamental was sent through a delay stage, which determines the time delay between the two pulses, and then was focused into a sapphire crystal, generating a white-light continuum. The pump pulse was sent through an optical chopper, reducing its frequency to 2.5 kHz. Both beams were then focused onto the sample. The probe light reflected off the mirror and was directed toward a charge-coupled device (CCD) (Helios, Ultrafast) (*34*).

XPS and UPS measurements

XPS and UPS measurements were conducted in PHI 5500 Multitechnique System with a base pressure of ~10^{-9} torr. The x-ray radiation was Al Kα emission (1486.7 eV; take-off angle, 75°). The UV radiation used in the UPS is helium Iα radiation, which has a photon energy of 21.22 eV. The take-off angle was 88°. A bias of −15 V was applied to measure the UPS spectra (*34*).

Characterization method

AFM measurements were performed with an Asylum Research Cypher AFM operated in alternating contact mode in air ambient condition. Imaging

Downloaded from http://advances.sciencemag.org/ on November 30, 2020

was done using ASYELEC-02 silicon probes with titanium-iridium coatings from Asylum Research. The probes had a typical spring constant of 42 N m^{-1}. XRD measurements were conducted using a Rigaku MiniFlex-6G 600 instrument (Bragg-Brentano geometry) equipped with D/teX Ultra silicon strip detector and a Cu Kα radiation source (λ = 1.5406 Å) operating at a voltage of 40 kV and a current of 15 mA. Attenuated total reflectance FTIR measurements were performed on a Thermo Nicolet is50. SEM images were taken on a Hitachi SU3500 490 instrument. ^{13}C and ^{1}H NMR spectra were measured using 500-MHz Agilent DD2 spectrometer equipped with a C134-senstive cryoprobe.

GIWAXS measurement

GIWAXS measurements were conducted at the Hard X-ray Micro-Analysis beamline of the Canadian Light Source. An energy of 17.998 keV (λ = 0.6888 Å) was selected using a Si(111) monochromator. Patterns were collected on a SX165 CCD camera (Rayonix) placed at a distance of 160 mm from the sample. A lead beam stop was used to block the direct beam. Images were calibrated using LaB6 and processed via the Nika software package and the GIXSGUI MATLAB plugin. For the in situ measurements, the precursor solution was deposited onto a cleaned glass substrate. The film was spun at 3000 rpm (the fastest speed allowed by the measurement geometry). After 12 s, toluene was dropped onto the spinning film. Data were collected every 1.7 s, and the films were allowed to spin for 2 min. The in situ GIWAXS measurement was conducted in ambient atmosphere. The precursor solutions remained in a nitrogen environment until just before the experiment to minimize the influence from ambient air. In addition, a small amount of metallic Sn powder was added to each precursor solution (with and without VA) to inhibit oxidation. The precursor solutions were filtered before deposition onto the substrate to remove the Sn powder.

Device fabrication and characterization

Low-conductivity ITO-coated glass substrates were cleaned by sonicating in deionized water and then in organic solvents (acetone then isopropyl alcohol), and then dried in an oven at 120°C for 10 min. The substrates were cleaned using a UV plasma treatment to enrich the ITO surface with oxygen and increase the ITO work function. The PEDOT:PSS HIL was spin coated at 6000 rpm (acceleration speed is 6000) for 20 s on the ITO followed by annealing in a nitrogen-filled glovebox at 150°C for 30 min. The emissive layer of PEA_2SnI_4 with a different concentration of precursors (PEAI and SnI_2 with or without VA) was spin coated via a two-step process, 1000 rpm for 10 s (accelerated speed is 200) and then 5000 rpm for 60 s (accelerated speed is 800). At the last 10 s in the second step, 300 μl of anti-solvent toluene was dropped quickly, followed by annealing in a nitrogen-filled glovebox at 100°C for 10 min to form the active emission layer. Last, the substrates were transferred to a vacuum chamber, and TPBI (60 nm) and LiF/Al electrodes (1 nm/150 nm) were deposited using a Kurt J. Lesker LUMINOS Cluster Tool evaporation system through a shadow mask under a high vacuum of less than 10^{-4} Pa. The device active area was 6.14 mm^2 as defined by the overlapping area of the ITO and Al electrodes. The luminance–current density–voltage characteristics were collected by using a HP4140B picoammeter. The absolute EL power spectra of the devices were collected using an integrating sphere and an Ocean Optics USB4000 spectrometer by mounting the devices on the wall of the integrating sphere. The EQEs were then calculated through the measured absolute power spectra and the current density (*34*). Three optimized batches of devices were fabricated for the statistics.

Stability measurements

LED stability was measured in a nitrogen-filled glovebox at room temperature under dark conditions without encapsulation. The devices were driven by a Keithley 2400 source meter at a constant current, and the luminance was measured using a commercial photodiode (Vishay Semiconductors BPW34). The photodiode was biased at 0 V, and the photocurrent was recorded at 2-s intervals. For the PL stability measurements, we first deposit a thin polymethyl methacrylate layer on the top of perovskite films. The films were removed from a nitrogen-filled glovebox every 10 days to measure the PL intensity under ambient conditions with humidity of ~30% and temperature ~25°C.

SUPPLEMENTARY MATERIALS

Supplementary material for this article is available at http://advances.sciencemag.org/cgi/content/full/6/42/eabb0253/DC1

REFERENCES AND NOTES

1. H.-W. Chen, R.-D. Zhu, J. He, W. Duan, W. Hu, Y.-Q. Lu, M.-C. Li, S.-L. Lee, Y.-J. Dong, S.-T. Wu, Going beyond the limit of an LCD's color gamut. *Light Sci. Appl.* **6**, e17043 (2017).
2. M. A. Baldo, D. F. O'Brien, Y. You, A. Shoustikov, S. Sibley, M. E. Thompson, S. R. Forrest, Highly efficient phosphorescent emission from organic electroluminescent devices. *Nature* **395**, 151–154 (1998).
3. D. J. Yu, F. Cao, Y. J. Gao, Y. H. Xiong, H. B. Zeng, Room-temperature ion-exchange-mediated self-assembly toward formamidinium perovskite nanoplates with finely tunable, ultrapure green emissions for achieving Rec. 2020 displays. *Adv. Funct. Mater.* **28**, 1800248 (2018).
4. K. Lin, J. Xing, L. N. Quan, F. P. G. de Arquer, X. Gong, J. Lu, L. Xie, W. Zhao, D. Zhang, C. Yan, W. Li, X. Liu, Y. Lu, J. Kirman, E. H. Sargent, Q. Xiong, Z. Wei, Perovskite light-emitting diodes with external quantum efficiency exceeding 20 per cent. *Nature* **562**, 245–248 (2018).
5. F. L. Yuan, S. H. Li, Z. T. Fan, X. Y. Meng, L. Z. Fan, S. H. Yang, Shining carbon dots: Synthesis and biomedical and optoelectronic applications. *Nano Today* **11**, 565–586 (2016).
6. X. Ai, E. W. Evans, S. Dong, A. J. Gillett, H. Guo, Y. Chen, T. J. H. Hele, R. H. Friend, F. Li, Efficient radical-based light-emitting diodes with doublet emission. *Nature* **563**, 536–540 (2018).
7. F. Yuan, Z. Wang, X. Li, Y. Li, Z. Tan, L. Fan, S. Yang, Bright multicolor bandgap fluorescent carbon quantum dots for electroluminescent light-emitting diodes. *Adv. Mater.* **29**, 1604436 (2017).
8. F. Yuan, T. Yuan, L. Sui, Z. Wang, Z. Xi, Y. Li, X. Li, L. Fan, Z. Tan, A. Chen, M. Jin, S. Yang, Engineering triangular carbon quantum dots with unprecedented narrow bandwidth emission for multicolored LEDs. *Nat. Commun.* **9**, 2249 (2018).
9. B. Zhao, S. Bai, V. Kim, R. Lamboll, R. Shivanna, F. Auras, J. M. Richter, L. Yang, L. J. Dai, M. Alsari, X.-J. She, L. S. Liang, J. B. Zhang, S. Lilliu, P. Gao, H. J. Snaith, J. P. Wang, N. C. Greenham, R. H. Friend, D. W. Di, High-efficiency perovskite-polymer bulk heterostructure light-emitting diodes. *Nat. Photonics* **12**, 783–789 (2018).
10. S. T. Zhang, C. Yi, N. Wang, Y. Sun, W. Zou, Y. Wei, Y. Cao, Y. Miao, R. Li, Y. Yin, N. Zhao, J. Wang, W. Huang, Efficient red perovskite light-emitting diodes based on solution-processed multiple quantum wells. *Adv. Mater.* **29**, 1606600 (2017).
11. Y. Tian, C. Zhou, M. Worku, X. Wang, Y. Ling, H. Gao, Y. Zhou, Y. Miao, J. Guan, B. Ma, Highly efficient spectrally stable red perovskite light-emitting diodes. *Adv. Mater.* **30**, 1707093 (2018).
12. X. Dai, Z. Zhang, Y. Jin, Y. Niu, H. Cao, X. Liang, L. Chen, J. Wang, X. Peng, Solution-processed, high-performance light-emitting diodes based on quantum dots. *Nature* **515**, 96–99 (2014).
13. T. Chiba, Y. Hayashi, H. Ebe, K. Hoshi, J. Sato, S. Sato, Y.-J. Pu, S. Ohisa, J. Kido, Anion-exchange red perovskite quantum dots with ammonium iodine salts for highly efficient light-emitting devices. *Nat. Photonics* **12**, 681–687 (2018).
14. J.-S. Yao, J. Ge, K.-H. Wang, G. Zhang, B.-S. Zhu, C. Chen, Q. Zhang, Y. Luo, S.-H. Yu, H.-B. Yao, Few-nanometer-sized α-$CsPbI_3$ quantum dots enabled by strontium substitution and iodide passivation for efficient red light emitting diodes. *J. Am. Chem. Soc.* **141**, 2069–2079 (2019).

Downloaded from http://advances.sciencemag.org/ on November 30, 2020

15. Y. Li, X. Hou, X. Dai, Z. Yao, L. Lv, Y. Jin, X. Peng, Stoichiometry-controlled InP-based quantum dots: Synthesis, photoluminescence, and electroluminescence. *J. Am. Chem. Soc.* **141**, 6448–6452 (2019).
16. H. Nakanotani, T. Higuchi, T. Furukawa, K. Masui, K. Morimoto, M. Numata, H. Tanaka, Y. Sagara, T. Yasuda, C. Adachi, High-efficiency organic light-emitting diodes with fluorescent emitters. *Nat. Commun.* **5**, 4016 (2014).
17. H. Ishiguro, K. Sawa, S. Nagao, H. Yamanaka, S. Koike, High efficient GaAlAs light-emitting diodes of 660 nm with a double heterostructure on a GaAlAs substrate. *Appl. Phys. Lett.* **43**, 1034 (1983).
18. R. Lin, K. Xiao, Z. Qin, Q. Han, C. Zhang, M. Wei, M. I. Saidaminov, Y. Gao, J. Xu, M. Xiao, A. Li, J. Zhu, E. H. Sargent, H. R. Tan, Monolithic all-perovskite tandem solar cells with 24.8% efficiency exploiting comproportionation to suppress Sn(ii) oxidation in precursor ink. *Nat. Energy.* **4**, 864–873 (2019).
19. X. Meng, J. Lin, X. Liu, X. He, Y. Wang, T. Noda, T. Wu, X. Yang, L. Han, Highly stable and efficient $FASnI_3$-based perovskite solar cells by introducing hydrogen bonding. *Adv. Mater.* **31**, 1903721 (2019).
20. H. Liang, F. Yuan, A. Johnston, C. Gao, H. Choubisa, Y. Gao, Y.-K. Wang, L. Sagar, B. Sun, P. Li, G. Bappi, B. Chen, J. Li, Y. Wang, Y. Dong, D. Ma, Y. Gao, Y. Liu, M. Yuan, M. Saidaminov, S. Hoogland, Z.-H. Lu, E. H. Sargent, High color purity lead-free perovskite light-emitting diodes via Sn stabilization. *Adv. Sci.* **7**, 1903213 (2020).
21. A. Waleed, M. M. Tavakoli, L. Gu, Z. Wang, D. Zhang, A. Manikandan, Q. Zhang, R. Zhang, Y.-L. Chueh, Z. Fan, Lead-free perovskite nanowire array photodetectors with drastically improved stability in nanoengineering templates. *Nano Lett.* **17**, 523–530 (2017).
22. J.-T. Lin, C.-C. Liao, C.-S. Hsu, D.-G. Chen, H.-M. Chen, M.-K. Tsai, P.-T. Chou, C.-W. Chiu, Harnessing dielectric confinement on tin perovskites to achieve emission quantum yield up to 21%. *J. Am. Chem. Soc.* **141**, 10324–10330 (2019).
23. V. Morad, Y. Shynkarenko, S. Yakunin, A. Brumberg, R. D. Schaller, M. V. Kovalenko, Disphenoidal zero-dimensional lead, tin, and germanium halides: Highly emissive singlet and triplet self-trapped excitons and X-ray scintillation. *J. Am. Chem. Soc.* **141**, 9764–9768 (2019).
24. S. Yakunin, B. M. Benin, Y. Shynkarenko, O. Nazarenko, M. I. Bodnarchuk, D. N. Dirin, C. Hofer, S. Cattaneo, M. V. Kovalenko, High-resolution remote thermometry and thermography using luminescent low-dimensional tin-halide perovskites. *Nat. Mater.* **18**, 846–852 (2019).
25. W.-L. Hong, Y.-C. Huang, C.-Y. Chang, Z.-C. Zhang, H.-R. Tsai, N.-Y. Chang, Y.-C. Chao, Efficient low-temperature solution-processed lead-free perovskite infrared light-emitting diodes. *Adv. Mater.* **28**, 8029–8036 (2016).
26. X. Zhang, C. Wang, Y. Zhang, X. Zhang, S. Wang, M. Lu, H. Cui, S. V. Kershaw, W. W. Yu, A. L. Rogach, Bright orange electroluminescence from lead-free two-dimensional perovskites. *ACS Energy Lett.* **4**, 242–248 (2019).
27. L. Lanzetta, J. M. Marin-Beloqui, I. Sanchez-Molina, D. Ding, S. A. Haque, Two-dimensional organic tin halide perovskites with tunable visible emission and their use in light-emitting devices. *ACS Energy Lett.* **2**, 16622–11668 (2017).
28. L. Ma, F. Hao, C. C. Stoumpos, B. T. Phelan, M. R. Wasielewski, M. G. Kanatzidis, Carrier diffusion lengths of over 500 nm in lead-free perovskite $CH_3NH_3SnI_3$ films. *J. Am. Chem. Soc.* **138**, 14750–14755 (2016).
29. Q. Tai, X. Guo, G. Tang, P. You, T.-W. Ng, D. Shen, J. Cao, C.-K. Liu, N. Wang, Y. Zhu, C.-S. Lee, F. Yan, Antioxidant grain passivation for air-stable tin-based perovskite solar cells. *Angew. Chem. Int. Ed.* **58**, 806–810 (2019).
30. F. Gu, S. Ye, Z. Zhao, H. Rao, Z. Liu, Z. Bian, C. Huang, Improving performance of lead-free formamidinium tin triiodide perovskite solar cells by tin source purification. *Sol. RRL* **2**, 1800136 (2018).
31. W. Xu, Q. Hu, S. Bai, C. Bao, Y. Miao, Z. Yuan, T. Borzda, A. J. Barker, E. Tyukalova, Z. Hu, M. Kawecki, H. Wang, Z. Yan, X. Liu, X. Shi, K. Uvdal, M. Fahlman, W. Zhang, M. Duchamp, J.-M. Liu, A. Petrozza, J. Wang, L.-M. Liu, W. Huang, F. Gao, Rational molecular passivation for high-performance perovskite light-emitting diodes. *Nat. Photonics* **13**, 418–424 (2019).
32. H. Hoshi, N. Shigeeda, T. Dai, Improved oxidation stability of tin iodide cubic perovskite treated by 5-ammonium valeric acid iodide. *Mater. Lett.* **183**, 391–393 (2016).
33. M. E. Kayesh, K. Matsuishi, R. Kaneko, S. Kazaoui, J.-J. Lee, T. Noda, A. Islam, Coadditive engineering with 5-ammonium valeric acid iodide for efficient and stable Sn perovskite solar cells. *ACS Energy Lett.* **4**, 278–284 (2019).
34. F. Yuan, Y.-K. Wang, G. Sharma, Y. Dong, X. Zheng, P. Li, A. Johnston, G. Bappi, J. Z. Fan, H. Kung, B. Chen, M. I. Saidaminov, K. Singh, O. Voznyy, O. M. Bakr, Z.-H. Lu, E. H. Sargent, Bright high-colour-purity deep-blue carbon dot light-emitting diodes via efficient edge amination. *Nat. Photonics* **14**, 171–176 (2020).
35. L. Zuo, H. Guo, D. W. deQuilettes, S. Jariwala, N. De Marco, S. Dong, R. DeBlock, D. S. Ginger, B. Dunn, M. Wang, Y. Yang, Polymer-modified halide perovskite films for efficient and stable planar heterojunction solar cells. *Sci. Adv.* **3**, e1700106 (2017).
36. A. B. Ponter, A. P. Boyes, The wetting properties of aqueous solutions of valeric acid on solid surfaces. *Can. J. Chem.* **50**, 1613–1616 (1972).
37. R. Quintero-Bermudez, A. Gold-Parker, A. H. Proppe, R. Munir, Z. Yang, S. O. Kelley, A. Amassian, M. F. Toney, E. H. Sargent, Compositional and orientational control in metal halide perovskites of reduced dimensionality. *Nat. Mater.* **17**, 900–907 (2018).
38. Z. Xiao, R. Kerner, L. Zhao, N. Tran, K. M. Lee, T.-W. Koh, G. D. Scholes, B. P. Rand, Efficient perovskite light-emitting diodes featuring nanometre-sized crystallites. *Nat. Photonics* **11**, 108–115 (2017).
39. X. Gong, O. Voznyy, A. Jain, W. Liu, R. Sabatini, Z. Piontkowski, G. Walters, G. Bappi, S. Nokhrin, O. Bushuyev, M. Yuan, R. Comin, D. McCamant, S. O. Kelley, E. H. Sargent, Electron-phonon interaction in efficient perovskite blue emitters. *Nat. Mater.* **17**, 550–556 (2018).
40. Y. Wang, R. Zou, J. Chang, Z. Fu, Y. Cao, L. Zhang, Y. Wei, D. Kong, W. Zou, K. Wen, N. Fan, N. Wang, W. Huang, J. Wang, Tin-based multiple quantum well perovskites for light-emitting diodes with improved stability. *J. Phys. Chem. Lett.* **10**, 453–459 (2019).

Acknowledgments

Funding: E.H.S. and all coauthors from the Department of Electrical and Computer Engineering at the University of Toronto acknowledge the financial support from the Ontario Research Fund–Research Excellence Program, the Natural Sciences and Engineering Research Council of Canada (NSERC), and the Global Research Outreach program of Samsung Advanced Institute of Technology. Z.-H.L. and all coauthors from the Department of Materials Science and Engineering at the University of Toronto acknowledge the financial support from the NSERC (grant number 216956-12) and the National Natural Science Foundation of China (grant number 11774304). Computations were performed on the Niagara supercomputer at the SciNet HPC Consortium. SciNet is funded by the Canada Foundation for Innovation, the Government of Ontario, Ontario Research Fund–Research Excellence, and the University of Toronto. **Author contributions:** E.H.S., Z.-H.L., and O.M.B. supervised the project. F.Y. and X.Z. conceived the idea and designed the experiments. F.Y. prepared the samples and fabricated the devices. X.Z. helped with the figure set and manuscript writing and provided helpful discussions and suggestions. A.J. measured the GIWAXS, processed the data, and helped with manuscript writing. Y.-K.W. conducted the AFM characterization. Y.D. measured and analyzed the fs-TA spectra. C.Z. and B.C. measured the SEM. P.L. and H.-T.K. measured the UPS and XPS. H.C. measured the XRD. J.Z.F. measured the FITR spectra. Y.G. helped with the analysis of fs-TA data. O.V. and G.S. helped with the discussions. F.Y. wrote the first draft of the manuscript. All authors discussed the results and contributed to the manuscript. **Competing interests:** The authors declare that they have no competing interests. **Data and materials availability:** All data needed to evaluate the conclusions in the paper are present in the paper and/or the Supplementary Materials. Additional data related to this paper may be requested from the authors.

Submitted 23 January 2020
Accepted 28 August 2020
Published 14 October 2020
10.1126/sciadv.abb0253

Citation: F. Yuan, X. Zheng, A. Johnston, Y.-K. Wang, C. Zhou, Y. Dong, B. Chen, H. Chen, J. Z. Fan, G. Sharma, P. Li, Y. Gao, O. Voznyy, H.-T. Kung, Z.-H. Lu, O. M. Bakr, E. H. Sargent, Color-pure red light-emitting diodes based on two-dimensional lead-free perovskites. *Sci. Adv.* **6**, eabb0253 (2020).

Downloaded from http://advances.sciencemag.org/ on November 30, 2020

Science Advances

Color-pure red light-emitting diodes based on two-dimensional lead-free perovskites

Fanglong Yuan, Xiaopeng Zheng, Andrew Johnston, Ya-Kun Wang, Chun Zhou, Yitong Dong, Bin Chen, Haijie Chen, James Z. Fan, Geetu Sharma, Peicheng Li, Yuan Gao, Oleksandr Voznyy, Hao-Ting Kung, Zheng-Hong Lu, Osman M. Bakr and Edward H. Sargent

Sci Adv **6** (42), eabb0253.
DOI: 10.1126/sciadv.abb0253

ARTICLE TOOLS http://advances.sciencemag.org/content/6/42/eabb0253

SUPPLEMENTARY MATERIALS http://advances.sciencemag.org/content/suppl/2020/10/09/6.42.eabb0253.DC1

REFERENCES This article cites 40 articles, 1 of which you can access for free
http://advances.sciencemag.org/content/6/42/eabb0253#BIBL

PERMISSIONS http://www.sciencemag.org/help/reprints-and-permissions

Use of this article is subject to the Terms of Service

Science Advances (ISSN 2375-2548) is published by the American Association for the Advancement of Science, 1200 New York Avenue NW, Washington, DC 20005. The title *Science Advances* is a registered trademark of AAAS.

Copyright © 2020 The Authors, some rights reserved; exclusive licensee American Association for the Advancement of Science. No claim to original U.S. Government Works. Distributed under a Creative Commons Attribution NonCommercial License 4.0 (CC BY-NC).

Downloaded from http://advances.sciencemag.org/ on November 30, 2020